Boundary conditions for electron tunneling in complex two- and three-dimensional structures

P. A. Sundqvist,* Q. X. Zhao, and M. Willander
Department of Physics, Göteborg University, Physical Electronics and Photonics, Fysikgränd 3, S-412 96 Göteborg, Sweden
(Received 11 May 2004; revised manuscript received 16 May 2005; published 7 October 2005)

We present boundary conditions given in integro-differential form for the single-particle two-dimensional (2D) or 3D Schrödinger equation, which allows for a treatment of nontrivial geometries, and an arbitrary number of input and output channels. The formalism is easy to implement using standard finite element packages. We consider a resonant dot structure and transport through a ringlike waveguide without barriers. The current in the dot is focused on an ellipsoid dot via a tunneling tip. The current-voltage characteristic is calculated for this system at the temperature 4.2 K. Our results show that the current maxima appear close to the eigenstates of the quantum dot. We show, however, that only those modes which obey certain symmetry properties give rise to resonance in the dot, and current maxima are absent for antisymmetric modes at low temperatures. The current in the waveguide is shown to be a resonant function of the voltage, and the system exhibits current feedback and turbulence. Finally, we extend the formalism to other types of channels and equations other than the Schrödinger equation and we discuss some possible applications for these systems.

DOI: 10.1103/PhysRevB.72.165103 PACS number(s): 72.10.Bg, 72.20.−i, 72.90.+y

I. INTRODUCTION

Advances in growth techniques have created a lot of theoretical interest in electron transport in low-dimensional structures. The interaction of the base region with the leads must be modeled accurately with the increasing miniaturization of devices. The scattering of an electron in 1D is the simplest scattering problem, and the current is dominated by the tunneling through resonant states as in a RTD (resonant tunneling diode[1]). The real system, however, contains the local atomic potential, scattering of various kinds, and many-body interactions. These effects can be treated by adding new terms to the single-particle Hamiltonian and by using a self-consistent Schrödinger-Poisson formalism.[2] However, when considering electronic transport in systems with higher dimensions using an effective mass approximation, the pure problem of wave transport becomes itself complicated. Hence, the fundamental study of electron scattering in low-dimensional (mesoscopic) structures has become a growing field in physics and many different approaches have been devised.

The formalism presented in this paper is based on wave function matching. We consider the interface surfaces between leads and a complex scattering region into boundary surfaces, and we show that the boundary conditions must be of an integro-differential type. The wave function matching method has been used extensively throughout the years, but it is not trivial in generaling the approach for an electron and/or hole traveling through a low-dimensional structure with an arbitrary shape and potential. Most calculations are for systems with high symmetry, for example, the calculation of electrons tunneling through quantum dots,[3] in which a lenslike dot with cylindrical symmetry was assumed. In addition, Mizuta and co-workers[4] performed a high symmetry three-dimensional numerical calculation on multimode quantum transport through a quantum dot including the phenomena of mode mixing. The symmetry allowed the wave function to be separated from the form $\varphi(x,y)\chi(z)$.

Tunneling through a nontrivial structure has been reported by Xia and Li[5] who studied electron wave transport through a circular planar quantum dot structure. The wave functions in the input and the output channels were matched to an analytic expansion of the wave function in the circular structure. Another interesting matching approach that allows for complicated structures has also recently been reported,[6] but relies on a finite difference treatment. This method allows, in principle, the study of complicated structures but with the constraint that the structure must consist of connected rectangular blocks.

The Landauer-Bütticker approach and advanced Green's functions methods are also commonly used to calculate electronic transport in mesoscopic systems and a good introduction of these methods is given in Ref. 7. Recently, a 2D finite element Greens functions method that included a density-functional treatment was presented by Havu *et al.*[8] The channels and the base region are represented by Green's functions and the boundary conditions are obtained through basis functions used in the numerics. The numerical Green's functions method has been generalized to consider multiterminal two- and three-dimensional systems.[9] The Green's functions were expressed in a numeric matrix form and contact block reduction was then applied. The Green's function was expanded in terms of the 3D eigenstates of the empty base region using Neumann boundary conditions towards the channels.

For a more complete overview we cite other tunneling approaches, which includes time-dependent methods[10–12] and density functional methods (DFT) methods.[13] The effect of spin polarization in quantum point contacts has also been studied by the use of the Kohn-Sham local spin-density formalism.[14]

The integro-differential boundary method used here differs from other numerical wave function matching methods in the sense that it can be integrated with commercially available finite element programs. Such programs often allow the user to draw the (complex) structure in a CAD (computer-aided design) environment where the potential and effective mass in different sub-domains (representing different material regions) can be defined without considering the internal boundary surfaces between these regions.

The energy levels in a quantum dot, although not all, as we shall show in this paper, are manifested as peaks in I-V characteristics. Therefore theoretical predictions can often be directly compared with measurements. Relevant experiments may include I-V measurements on planar tunneling devices (e.g., Jung[15] and co-workers). A similar experiment for a three-dimensional tunneling transistor has been performed by Lind *et al.*[16] In addition, there have been reports on one-dimensional RTD's (Refs. 17 and 18) and zero-dimensional RTD's.[19–21]

This paper is organized as follows: In Sec. II we first develop the overall theory for the boundary conditions for cylinder shaped input and output channels. Next, we generalize the concept of channels and give an example of plane wave scattering in 2D. Thereafter we describe also how to derive integro-differential boundary conditions for types of equations other than the Schrödinger equation, illustrated by a Poisson equation example in 2D. In the Sec. II D we finally derive the expression for the total current using standard thermal statistics. The results of two different applications of the tunneling theory in two dimensions are presented in Sec. III. Section IV is devoted to conclusions. In the Appendix we give some details of the integro-differential boundary conditions and of the numerical procedure, where we show how to implement these for a simple case but also in the specific FEMLAB software (Ref. 23).

II. THEORY

The following section is divided up into four subsections. In Sec. II A we develop the boundary conditions for input and output channels with general cylinder shapes in two and three dimensions. Next, in Sec. II B we present the boundary conditions for plane-wave scattering in 2D. Section II C explains, through a Poisson equation example, how the matching technique that results in integro-differential boundary conditions is not uniquely valid only for the Schrödinger equation. In Sec. II D we give the derivation of the total current.

A. Tunneling theory

We consider the time-independent single-electron problem and derive boundary conditions for input and output channels where the scattering region can be arbitrary shaped. The matching of various scalar fields (such as a wave function) and their normal derivatives at the boundaries between the channels (leads) and the scattering region (sample) is well known.[7,22] In our case this matching results in integro-differential boundary conditions (which are unusual) and for the sake of clarity we therefore present a detailed derivation. Explicitly, the derived boundary conditions are input into a commercial finite element software, which is suitable for treating arbitrary complex scattering domains and which generates a numerical grid.

Since we treat a tunneling problem, i.e., an open system, the Schrödinger equation is not an eigenvalue problem, but takes the form of the Helmholtz equation

$$-\frac{\hbar^2}{2}\nabla\cdot\left(\frac{1}{\tilde{m}(\vec{r})}\nabla\Psi(\vec{r})\right)+[V(\vec{r})-E]\Psi(\vec{r})=0, \qquad (1)$$

where E is the energy (an invariant for the whole system), $\tilde{m}$ is the effective mass tensor, and $V(\vec{r})$ is the potential energy in the structure. We consider the mass as piecewise isotropic and constant but the analysis could easily be modified to take the anisotropy into account, if needed. It is also instructive to consider Eq. (1) in a scaled form, together with the local wave number k as

$$\nabla^2\Psi(\vec{r})+k^2(\vec{r})\Psi(\vec{r})=0, \qquad (2)$$

$$k^2(\vec{r})=\frac{2ma^2}{\hbar^2}[E-V(\vec{r})], \qquad (3)$$

where a is a scaling constant for the space coordinate $\vec{r}$ of the system (thus $\vec{r}$ and k are both dimensionless). When $V(\vec{r})=0$ the solution is a plane wave $\exp(\pm i\vec{k}\cdot\vec{r})$.

The intricate part of the analysis of the wavelike solution of Eq. (2) [when $V(\vec{r})\neq 0$] are the boundary conditions. Our goal is to calculate the quantum current through an arbitrary three-dimensional (3D) scattering region and the way we can do this is by introducing input and output channels connected to the scattering region. The concept of incoming and outgoing channels (leads) with simple properties is not new and has been applied extensively for the treatment of transport through mesoscopic systems (Landau-Büttinger approach).[7]

The channels have to be general cylinders, similar to the cylinders shown in Fig. 1. The potential inside these cylinders must be separable of the kind $V(\vec{r})=V(x,y)+V_0$, and no dependence on z is allowed inside the channels. For convenience we assume that the wave propagates in the z direction and that the wave function is confined in the x-y plane (we will use the Cartesian coordinate system rather than $\vec{r}_\perp$ and $\vec{r}_\parallel$ for the rest of this paper). The boundary condition on the channel surface is the homogeneous Dirichlet boundary condition i.e., $\Psi=0$. The length of the cylinders are semi-infinite to allow wave solutions in the z direction. In connection with the scattering region the cross section surface must be flat (i.e., no curvature of the surface). The effective mass should satisfy $m_{ij}=m_{0i}\delta_{ij}$, where m_{0z} is a constant and where m_{0x} and m_{0y} are functions of x and y only.

For each channel (either input or output), we are interested in the eigenfunctions φ_j and the corresponding eigenvalue λ_j, determined from the geometry and the equation

$$-\nabla^2\varphi_j(x,y)=\lambda_j\varphi_j(x,y). \qquad (4)$$

This equation is also dimensionless, or in other words, scaled with a. In an input channel we could express the complete wave solution (here denoted with the index $r1$ for channel 1) as

$$\Psi_{r1}=e^{ik_\mu(z-z_1)}\varphi_\mu(x,y)+\sum_j r_j e^{-ik_j(z-z_1)}\varphi_j(x,y), \qquad (5)$$

where z_1 is the coordinate for the interface between input channel 1 and the scattering region. The subscript μ indicates the mode of the incoming wave [for example, the ground state mode $\varphi_0(x,y)$]. The reflected waves (negative

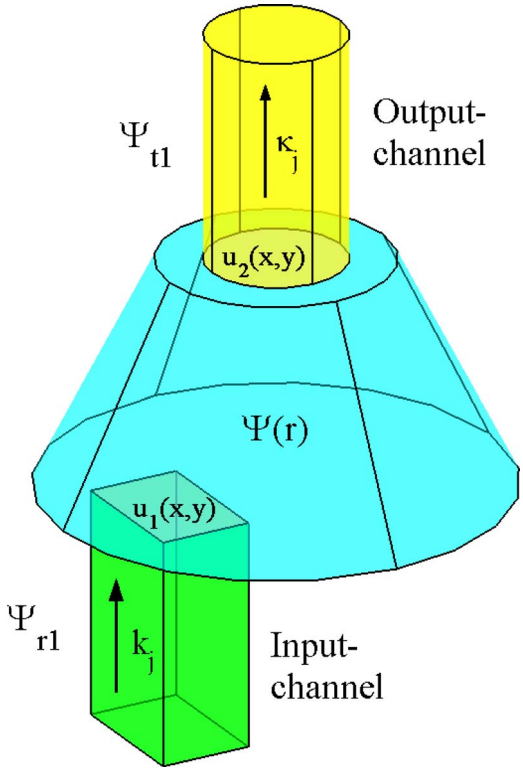

FIG. 1. (Color online) The rectangular cylinder is the input channel (of infinite length) and is described by a wave function Ψ_{r1} and wave numbers k_j. The circular cylinder is the output channel in where we have a wave function Ψ_{t1} and wave numbers κ_j. The input- and output-boundary surfaces of the complex structure (the conical volume in this case) are denoted as $u_1(x,y)$ and $u_2(x,y)$.

sign in the exponential) are weighted with the reflection coefficient r_j for the jth mode, respectively. Indeed, the wave function Ψ_{r1} in Eq. (5) is a solution to Eq. (2) if we demand that k_j must satisfy the relation

$$k_j^2 = \frac{2m_1 a^2}{\hbar^2}(E - V_1) - \lambda_j, \tag{6}$$

where V_1 is a constant potential in channel 1 (not included in λ_j) and m_1 is the effective mass in channel 1. For example, we may use the potential difference ΔU between a source and a drain contact so that $V_1 = V_S$ and $V_2 = V_D$ and $e\Delta U = V_S - V_D$. For small values of the energy E and for higher modes, k_j could hence be imaginary and represent decaying solutions so that $|\Psi| \to 0$ when $|z| \to \infty$.

The solution Ψ in Eq. (2) and its derivative with respect to the plane normal coordinate (in this case z) should be matched at z_1. We denote the scattering space with Ω and boundaries to it with $\partial\Omega_i$. At the boundary surface $\partial\Omega_1$ (the surface toward the input channel) is denoted as $u_1(x,y)$ to avoid confusion with Ψ, i.e., $\partial\Omega_1$ is a subspace of Ω and hence $u_1(x,y)$ is a subset of $\Psi(\vec{r})$ (see Fig. 1). The matching condition $\Psi_{r1} = u_1$ at $z = z_1$ reads then

$$u_1(x,y) = \varphi_\mu(x,y) + \sum_j r_j \varphi_j(x,y). \tag{7}$$

We must also match the normal derivative on the boundary by the equality

$$\frac{1}{m_{\partial\Omega_1}} \hat{n} \cdot \nabla u_1 \Big|_{z_1} = \frac{1}{m_1} \hat{n} \cdot \nabla \Psi_{r1} \Big|_{z_1}, \tag{8}$$

where $m_{\partial\Omega_1}$ is the effective mass inside Ω close to channel 1 and m_1 is the effective mass in channel 1. In this case $\hat{n} = -\hat{z}$ so we get

$$\frac{1}{m_{\partial\Omega_1}} \hat{n} \cdot \nabla u_1 = -\frac{1}{m_1} \frac{\partial \Psi_{r1}}{\partial z} = \frac{1}{m_1}\left(-ik_\mu \varphi_\mu(x,y) + \sum_j ik_j r_j \varphi_j(x,y)\right). \tag{9}$$

On this form all r_j are unknown and we therefore take advantage that φ_j is an orthonormal and a complete set to determine r_j in terms of $u_1(x,y)$. By multiplying Eq. (7) from the left with $\varphi_i^*(x,y)$ and integrating over $\partial\Omega_1$ we finally obtain

$$r_j = -\delta_{\mu,j} + \int \varphi_j^*(x,y) u_1(x,y) dx\, dy. \tag{10}$$

We take this expression for r_j and insert it into Eq. (9) to obtain an integro-differential boundary condition

$$\hat{n} \cdot \nabla u_1 = \left(\frac{m_{\partial\Omega_1}}{m_1}\right)\left(-2ik_\mu \varphi_\mu(x,y) + \sum_j ik_j \tilde{u}_{1,j} \varphi_j(x,y)\right), \tag{11}$$

where $\tilde{u}_{1,j}$ is the jth Fourier component of $u_1(x,y)$ in terms of the basis functions $\varphi_j(x,y)$

$$\tilde{u}_{1j} = \int \varphi_j^*(x,y) u_1(x,y) dx\, dy. \tag{12}$$

Equation (11) is the boundary condition used in finite element software programs. It is an integro-differential boundary condition in the sense that it contains both a derivative and surface integrals [Eq. (12)] but it is similar to the general Neumann boundary condition $-\hat{n} \cdot \nabla u + bu = g$, where b and g are coefficients and where g is a source term. In the Appendix we give a more detailed comparison between the Neumann boundary condition and the derived integro-differential boundary conditions and we also compare them with Green's functions.

The first term on the right-hand side of Eq. (11) is the source term for the wave solution of the Helmholtz equation. Without the source term, the solution of the Helmholtz equation in the 3D scattering region would be trivial, i.e., $\Psi(\vec{r}) = 0$. The sum is a linear expression in terms of the discrete and numeric $u_1(x,y)$; the problem is purely linear. By combining Eq. (12) with Eq. (10) we could express the reflection coefficients in terms of the Fourier components as

$$r_j = -\delta_{\mu,j} + \tilde{u}_{1,j}. \tag{13}$$

Matching of wave functions and their derivatives assumes normally that the wave function is known at one place, but

this is not the case here since the wave function is unknown on *both* sides (i.e., the reflection coefficients are unknown, and must be "removed" by the orthogonal integration trick). This method could also be seen as a generalization of the transfer matrix method used for one-dimensional structures (see, for instance Ref. 22).

The boundary condition could also be treated for a 2D problem, if we instead consider $u_1(y)$ and the corresponding integration over a boundary line instead of an area ($\partial\Omega_1$). In 1D the corresponding boundary condition (where the input boundary is a point, described by the scalar u_1) reads

$$-\frac{du_1}{dz} = \left(\frac{m_{\partial\Omega_1}}{m_1}\right)(-2ik_1 + ik_1u_1). \tag{14}$$

We now analyze the boundary conditions for an output channel. A complete wave solution in an output channel (here denoted by the index $t1$) has the form

$$\Psi_{t1} = \sum_j t_j e^{i\kappa_j(z-z_2)}\phi_j(x,y), \tag{15}$$

where the outgoing waves (positive sign in the exponential) are weighted with transmission coefficients t_j for the jth mode, respectively. Here we choose the basis set $\phi_j(x,y)$ and wave numbers κ_j to distinguish from the input channel, since the output channel could have a different shape as well as a different potential offset V_2 (see Fig. 1). The basis functions ϕ_j, the eigenvalues $\lambda_j^\star$ and wave numbers κ_j are determined from

$$-\boldsymbol{\nabla}^2\phi_j(x,y) = \lambda_j^\star\phi_j(x,y), \tag{16}$$

$$\kappa_j^2 = \frac{2m_2a^2}{\hbar^2}(E - V_2) - \lambda_j^\star, \tag{17}$$

where m_2 is the effective mass in channel 2.

Denoting the wave function at the output boundary $\partial\Omega_2$ as $u_2(x,y)$ we obtain after some steps the integro-differential boundary condition of output type

$$\hat{n}\cdot\boldsymbol{\nabla}u_2 = \left(\frac{m_{\partial\Omega_2}}{m_2}\right)\left(\sum_j i\kappa_j\tilde{u}_{2,j}\phi_j(x,y)\right), \tag{18}$$

where $\tilde{u}_{2,j}$ is the jth Fourier component of $u_2(x,y)$ in terms of the basis functions $\phi_j(x,y)$ [compare with Eq. (12)]. The transmission coefficients t_j are in this case given by

$$t_j = \tilde{u}_{2,j}. \tag{19}$$

In one dimension the corresponding Neumann boundary condition is given by

$$\frac{du_2}{dz} - i\kappa_2u_2\left(\frac{m_{\partial\Omega_2}}{m_2}\right) = 0, \tag{20}$$

where the output boundary is a point, described by the scalar u_2. In the 1D case [see Eqs. (14) and (20)] we assume the input wave to be $\exp[ik_1(z-z_1)]+r\exp[-ik_1(z-z_1)]$ and the output wave to be: $t\exp[i\kappa_2(z-z_2)]$. When the solution (which includes u_1 and u_2) has been obtained we can calculate the reflection and the transmission coefficients as $r=u_1-1$ and $t=u_2$. For some cases this method is better suited than the transfer matrix method since the local $k(z)$ in the transfer matrix method causes singularities for some types of potentials (resonant tunneling potentials, for example) and as well as for long wavelengths (the solution by the transfer matrix method gives normally numerical errors in this limit). Note that the well-known tunneling through a barrier problem easily could be solved with this method using the boundary conditions described above and without the matching of wave functions (this is already included in the boundary conditions).

The solution of Eq. (2), together with the boundary conditions given in Eqs. (11) and (18) is unique. The solution $\Psi(\vec{r})$ incorporates as well the boundary functions u_1 and u_2. These functions could then be decomposed into their Fourier components, i.e., we could obtain r_j and t_j from u_1 and u_2. Further on this means that we also have the full solution of the whole system, not only in the scattering region, but also in the input and the output channel. For this purpose we use Eqs. (5) and (15), where it should be noted that these expressions are defined using the specific z dependence relative to the adjacent surface normal. Generally, we should replace $\exp(-ik_j(z-z_1))$ with $\exp[ik_j\hat{n}\cdot(\vec{r}-\vec{r}_1)]$ for an input channel and we should use $\exp(-i\kappa_j\hat{n}\cdot(\vec{r}-\vec{r}_2))$ for an output channel, where we define the plane normal $\hat{n}$; we point outward towards the boundary of the inner scattering geometry.

It is of crucial importance that all eigenfunctions are normalized to unity, since the whole derivation is made with this assumption. Also, the complex conjugate of the normalized basis functions, used in the expressions for $\hat{u}_{1j}$ and $\hat{u}_{2j}$, is also important to keep in the 3D case (when, for example, the eigenfunctions could be found to be analytical complex functions).

Note here that there is no coordinate dependence on any of the boundary conditions. This implies that our system is invariant under translation and rotation. We could therefore safely consider a channel coming in or out from any direction and not only from the z direction. The important property of a channel is its cross-section eigenvalues and eigenfunctions (which also are independent of rotation and translation).

Finally the normalization of the wave function is of interest. Consider that the input and the output channel have the length L in dimensionless units, which in turn must tend to infinity as we assume plane-wave solutions in the z direction. It is thus evident that the integral of $|\Psi|^2$ in the scattering region (Ω) will be relatively small in comparison with the normalization integrals in the channels if $L\to\infty$. The total normalization integral N is then (here for the case when we only have one input channel and one output channel) given by

$$N = a^3L\left(1 + \sum_j[|r_j|^2 + |t_j|^2]\right). \tag{21}$$

The factor a^3 stems from scaling and L (dimensionless) will however disappear when the total current is summed up, as will be shown in Sec. II D. When the numerical solution has been found, the quantum current density $\vec{j}(\vec{r})$ could be

calculated (and be visualized) directly by using the well-known expression

$$\vec{j}(\vec{r}) = -\frac{e\hbar}{m(\vec{r})aN}\,\mathrm{Re}\{i\Psi^*(\vec{r})\,\boldsymbol{\nabla}\,\Psi(\vec{r})\}, \tag{22}$$

where e is the charge of the electron, $m(\vec{r})$ is the coordinate dependent effective mass, a is the coordinate scaling parameter, and N is given from Eq. (21). Finally, the procedure to include more than one input and output channel is straight forward, even if the physical interpretation of how an electron has its source from two different infinite channels seems to be absurd. However, interesting interferometry phenomena may be studied by introducing a phase difference between two input channels for a similar electromagnetic problem.

B. Plane-wave scattering

In Sec. II A we gave the boundary condition for cylinder shaped channels. To illustrate the generality of the wave matching method we show here how this technique could be used to treat plane-wave scattering in 2D.

The idea is to enclose the complex scattering region, also including an arbitrary potential $V(\vec{r})$ within a circle, say with radius R. Outside this radius we assume $V(\vec{r})=0$ and we here have an incoming plane wave given by $\exp(ik_1x)$, where k_1 is the wave number determined from the energy relation $k_1 = \sqrt{2mE/\hbar^2}$.

Using the Jacobi-Anger expansion of a plane wave we could write the wave function outside the radii, Ψ_1, as

$$\Psi_1(\rho,\alpha) = \sum_{\mu=-\infty}^{\infty} [i^\mu J_\mu(k_1\rho) + r_\mu H_\mu^{(1)}(k_1\rho)]e^{i\mu\alpha}, \tag{23}$$

where r_μ is the μth reflection coefficient, J_μ are the Bessel functions, and $H_\mu^{(1)}$ are the outgoing Hankel functions, valid for $\rho \geqslant R$. The angle α in the x-y plane is defined so that $x = \rho\cos(\alpha)$, etc. Denoting the numerical solution of $\Psi(\vec{r})$ at the boundary ($\rho=R$) as $u(\alpha)$ we match it with the wave function in Eq. (23) and we also match their normal derivatives (with respect to ρ). The same procedure as in Sec. II A results in the integro-differential boundary condition

$$\hat{n}\cdot\boldsymbol{\nabla}u = \sum_{\mu=-\infty}^{\infty} k_1[i^\mu J_\mu'(k_1R) + r_\mu H_\mu^{(1)\prime}(k_1R)]e^{i\mu\alpha}, \tag{24}$$

where the reflection coefficients are given by

$$r_\mu = \frac{\tilde{u}_\mu - 2\pi i^\mu J_\mu(k_1R)}{2\pi H_\mu^{(1)}(k_1R)}, \tag{25}$$

and where finally the Fourier components $\tilde{u}_\mu$ are defined by

$$\tilde{u}_\mu = \int_0^{2\pi} e^{-i\mu\alpha}u(\alpha)d\alpha. \tag{26}$$

It is also possible to combine different types of channels, depending on the specific geometry of interest (in 2D, semicircles and lines and in 3D, semispheres and cylinders). The second term on the right-hand side of Eq. (23) represents a scattered wave. The reflected terms could be used to estimate the angular-dependent magnitude of the echo from an arbitrary object, given a pulsed incoming signal, even though this, in principle, is a time-dependent problem.

C. Other equation types

The technique to derive integro-differential boundary conditions for the Schrödinger equation could also be adopted for other equations such as the Maxwell's wave equations, acoustic wave equations, and Poisson's equation to name some examples. In fact, the technique could be used for any type of partial differential equation (PDE) if a complete analytic expansion exist in a semi-infinite space. To illustrate this we give a simple example where we derive integro-differential boundary conditions for Poisson's equation in 2D.

Consider a complex charge distribution between two grounded plates in 2D separated by a distance of b, $(0<x<b)$. We demand that the electric potential should approach towards zero as $|y|\to\infty$. If the charge distribution (and possibly also additional inner boundaries), are kept within the domain $-d<y<d$, we only have to solve the PDE within this domain, but with boundary conditions at $y=\pm d$ that are similar to those described in Sec. II B. The electric potential ϕ_1 in the region $y>d$ is then given by

$$\phi_1(x,y) = \sum_n r_n \sin\left(\frac{n\pi x}{b}\right)e^{-k_n(y-d)}, \tag{27}$$

where $k_n = n\pi/b$ to fulfill the solution of the charge-free Poisson equation for each term and where r_n are coefficients. Denoting the numerical solution at the boundary $y=d$ as $u_1(x)$ we obtain the boundary condition

$$\hat{n}\cdot\boldsymbol{\nabla}u_1(x) = \sum_n -k_n\tilde{u}_n \sin\left(\frac{n\pi x}{b}\right), \tag{28}$$

where $\tilde{u}_n$ and r_n are given by the Fourier components of $u_1(x)$ in terms of the x-dependent basis functions as

$$\tilde{u}_n = r_n = \frac{1}{\sqrt{b}}\int_0^b u_1(x)\sin\left(\frac{n\pi x}{b}\right)dx. \tag{29}$$

The boundary condition at $y=-d$ is similar. The inner region could contain inner boundary regions with arbitrary boundary conditions as well, since they are treated by the numerical solver program (FEMLAB, for instance).

An interesting application of this method is the Coulomb integral problem. For a charge distribution that is restricted within a certain radius one could obtain the electric potential by solving Poisson's equation numerically, without sticking into the image charge problem (by use of the spherical harmonics).

D. Thermal statistics of total current

In the derivation of the total current, which is obtained by the use of the Fermi-Dirac statistics, we assume noninteract-

ing electrons. A more precise treatment would be to include a self-consistent potential field arising from the electronic charge density in the structure. In that case we must perform a self-consistent 3D Schrödinger-Poisson calculation. We ignore this phenomenon here since we want to focus on the tunnel mechanisms in this paper.

With the noninteracting electron assumption, the total current $I(E)$ in the outgoing channel, contributed from a single electron, with the energy E, is obtained by integrating the z component of $\vec{j}(\vec{r})$ over the channel surface. Using orthonormality of the basis functions we obtain

$$I(E) = \int \vec{j} \cdot d\vec{S} = \frac{e\hbar a}{m_2 N} \sum_j |t_j|^2 \, \mathrm{Re}\{\kappa_j\}. \tag{30}$$

Note that the wave vectors κ_j also are dimensionless. Both presented expressions in the above equation could be used, since we know the current density numerically [see Eq. (22)]. The normalization constant N involves the length L of the incoming channel. Hence, the factor $1/L$ could be interpreted as a line density for one electron. However, when we sum up the current from all free electrons in the channels, we should rather use the Fermi-Dirac statistics to respect the Pauli principle. The standard procedure is to perform the following replacement:

$$\frac{1}{L} \to 2 \int \left(\frac{dk}{2\pi} \right). \tag{31}$$

The factor 2 stems from spin degeneracy. More precisely, we also include the Fermi-Dirac distribution f, containing the Fermi energy E_F and the temperature T. We must also sum over all eigenmodes in the channel. Particle conservation results then in the following equation for the Fermi energy:

$$\pi a^3 A n = \sum_j \int_0^\infty \frac{dk}{\exp[(\lambda_j + k^2 - \varepsilon_F)/\eta] + 1}, \tag{32}$$

where A is the area of the channel in dimensionless units, n is the electron density in bulk, and $\eta = 2m_1 a^2 k_B T/\hbar^2$ is a dimensionless temperature. The Fermi energy is also scaled here for simplicity, i.e., $E_F = \hbar^2 \varepsilon_F / 2m_1 a^2$. At $T=0$ K we obtain the simplification

$$\pi a^3 A n = \sum_j \sqrt{\varepsilon_F - \lambda_j}\, \Theta(\varepsilon_F - \lambda_j), \tag{33}$$

where $\Theta(x)$ is the unit step function. This expression is easy to draw by hand, and it can be used to graphically estimate the numerical solution of ε_F. If the number on the left-hand side is small (i.e., if $\pi a^3 A n < \sqrt{\lambda_2 - \lambda_1}$) we only need to integrate up k in the first subband in the expression for the total current. But if it has a larger value, more subbands have to be included (even at $T=0$ K). For small, but finite temperatures, the graph is smooth so that we may need to take the first two subbands into account and so on.

When the Fermi level has been found, the current can easily be obtained. For a case where the structure is very thin, i.e., an effective two-dimensional system, the total current is given by

$$I = \frac{e\hbar}{m_1 a^2} \sum_j \int_0^\infty \frac{I(k)dk}{\exp[(\lambda_j + k^2 - \varepsilon_F)/\eta] + 1}, \tag{34}$$

where $I(k)$ is the dimensionless surface integral (i.e., line integral for two dimensions) of the current density at the incoming (or outgoing) channel if we omit the factor $a^3 L$, but keep the normalization sum in Eq. (21) and omit the factor $e\hbar/m$ in the current density expression [See Eq. (22)].

In the given expression for the total current we ignore the backward current from the output to the input channel. The arguments for this approximation are the following; (i) The temperature is low. (ii) The current is small everywhere except at certain applied voltages where current resonance appears. Physically we must have $I=0$ at $V=0$, but since the current given in Eq. (34) is extremely small at $V=0$ (far from resonance) we can ignore the influence of the backward current. The backward current will only be significant in the thermal energy range, which corresponds to 0.3 mV for $T=4.2$ K. We will show in the result section that the first resonant current peak in the I-V characteristic will appear first at approximately 50 mV, which is hence far away from 0.3 mV.

III. RESULTS

The result section is divided into two subsections. In Sec. III A we present numerical results for electron transport through a ringlike waveguide structure. In Sec. III B we present results of resonant electron tunneling through a structure with a sharp tunnel tip and a quantum dot.

A. Transport through a ringlike waveguide structure

The structure we study here is shown in the upper part of Fig. 2 (in dimensionless units), where the horizontal and vertical axis are referred to as the x and the y axis, respectively. An electronic wave is assumed to be injected at the top of the left side and a transmitted wave is assumed to exit at the top of the right side. The steady state currents, i_0, i_a, and i_b, are shown with arrows in the figure. Kirchhoff's first law for the node at the left side (i.e., close to the point $x=-1.5$ and $y=-0.5$ in Fig. 2) is given by $i_0 = i_a + i_b$ and at the right node ($x=1.5$ and $y=-0.5$) it is given by $i_a + i_b = i_0$, using the directions shown in the picture. Note also that input current (i_0) equals output current, i.e., influx equals outflux. In the lower part of Fig. 2 the real part of the electronic wave function is shown for a case when an electron is accelerated through a linear potential drop between the input and the output channel. The situation is clearly analog to the case of an electromagnetic wave propagating through a waveguide.

The voltage drop through the structure is obtained by solving the Laplace equation. The obtained potential is then coupled to the Schrödinger equation numerically. In a real situation, we have to calculate charges in the structure and solve Poisson's equation self-consistently with the wave solution of the Schrödinger equation for all energies of occupied states. However, we ignore this phenomenon here, since we want to focus on the transport mechanism. Therefore, we mimic the potential by the following assumptions: (i) The

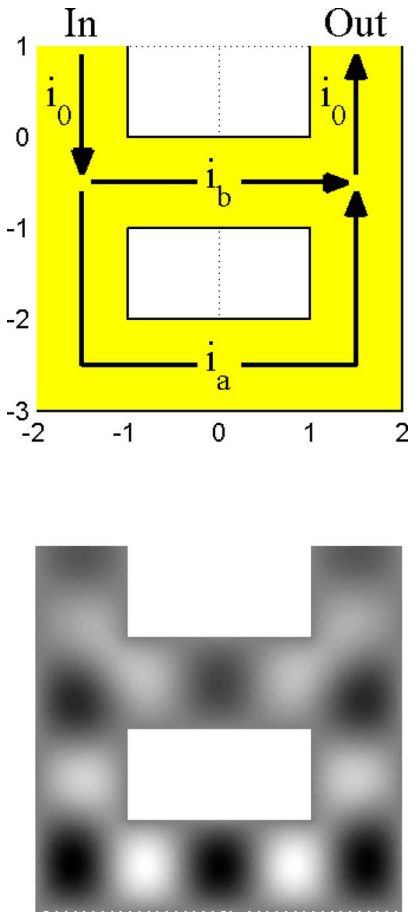

FIG. 2. (Color online) The upper figure shows the structure with incoming and outgoing current i_0. The x and the y axis are oriented horizontally, respectively, vertically in the figure. The arrows labeled i_a and i_b indicate currents in the lower and the upper branch, respectively. The lower figure shows the real part of the wave function Ψ for a low voltage bias ($V=0.2$). The grayscale ranges from black [$\mathrm{Re}(\Psi)=-1$] to white [$\mathrm{Re}(\Psi)=+1$]. $\mathrm{Re}(\Psi)=0$ corresponds to "medium" gray, also valid for the boundary where $\Psi=0$.

input surface is grounded and at the output boundary we set the potential to $-V$, where the applied voltage V is varied for different calculations (a positive voltage bias). (ii) On all other boundaries in the structure we apply homogenous Neumann boundary conditions (in conductive media electrostatics this corresponds to zero current through the walls).

For the wave function we use a homogenous Dirichlet boundary condition on the rectangle in the middle, representing hard walls. In principle, we can replace this region by a region with a high barrier, but it is our intention to define our system in this way for two reasons. First, we want to show that our model can treat inner boundaries with arbitrary shapes. This is an advantage of our approach that we want to emphasize. Second, this opportunity allows us to reduce our numerical grid essentially. The outer boundaries are also of the Dirichlet type.

The geometry, the Schrödinger equation, the energy, and the voltage are all scaled (i.e., they are dimensionless) to be of the order of unity.

For the analysis of this subsection we introduce the concept of current gain, denoted G and current feedback, denoted β. Based on our numerical result, we find that the current may circulate clockwise or counter clockwise in the circuit at certain ranges of the energy and the voltage biasing. In other parameter regions, the incoming current i_0 is only "classically" divided into i_a and i_b. The phenomenon of feedback in the structure is possible because of wave function coherence, but it is not easy to understand from a simplified signal model. Therefore we introduce the concept of feedback phenomenologically. For the case of counter clockwise current circulation we assume that the current i_b is a fraction of the current i_a given as $i_b=-\beta i_a$, where the minus sign indicates an opposite direction. The feedback fraction β is strongly dependent on the wavelength and the voltage drop in the structure. Further on, we define the gain as $G=i_a/i_0$. Combining Kirchhoff's first law and the definitions of G and β we obtain $G=1/(1-\beta)$. Thus if $\beta=0.99$ (99% feedback) we obtain a gain $G=100$. This means that i_a is a factor 100 times larger than the incoming current and that i_b is 99 times larger than i_0. The same discussion can be applied to turbulence phenomena, obtained in our calculations as well.

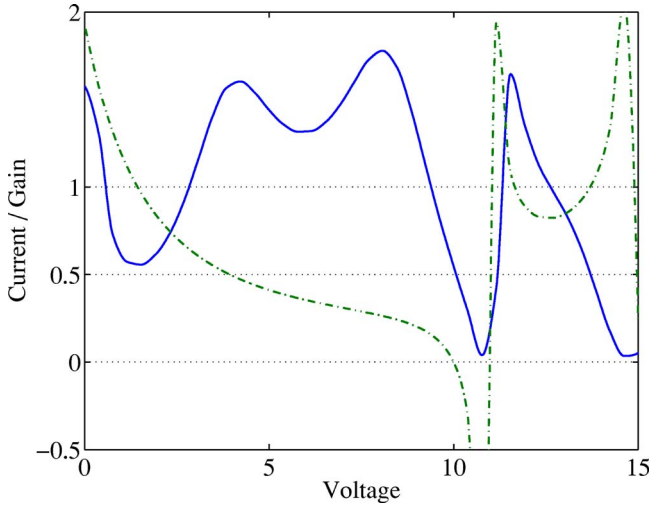

FIG. 3. (Color online) Total current (i_0, solid line) and gain (G, dash-dotted line) vs applied voltage. The current is a resonant function of the voltage. The gain is changing sign abruptly at $V\approx 10.8$, where $i_0\cong 0$. For $G<0$ and $G>1$, the current circulates clockwise or counter clockwise, respectively (see Fig. 2).

By plotting the gain as a function of the voltage we obtain information of whether there is circular current or not. In the range $0<G<1$ ($\beta<0$) we have no feedback and the incoming current i_0 is divided into i_a and i_b. If $G\geqslant 1$ ($0<\beta<1$) the current circulates counter clockwise and finally if $G\leqslant 0$ ($\beta\geqslant 1$) the current circulates clockwise.

In Fig. 3 the current and the gain are plotted as a function of the voltage. All results are given in dimensionless units. The energy is kept fixed for this calculation and is equal to the mean value of the first and the second eigenvalue of the boundary, $\varepsilon=(\lambda_1+\lambda_2)/2$ [See Eq. (4)]. The incoming wave is assumed to be in the ground state mode, which is true for low temperatures and moderate doping levels in the input channel. For a large bias voltage we get a long wavelength in the input channel and a short wavelength in the output channel [i.e., compare Eq. (6) and Eq. (17)]. We see that the

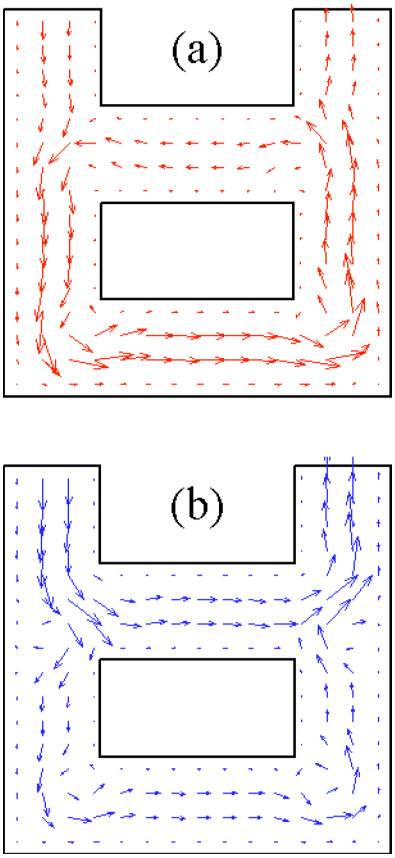

FIG. 4. (Color online) (a) Current density shown for a low voltage bias ($V=0.2$) where the current in the lower branch (i_a, see Fig. 2) is larger than the incoming current (i.e., positive feedback $G>1$). Arrow lengths are proportional to current density. (b) Current density shown for $V=4.8$, where the incoming current is divided equally between i_a and i_b.

current is a resonant function of the voltage, which could be understood if we look upon the structure in Fig. 2 as a resonant "cavity" with certain resonant modes. In this calculation, we keep the energy fixed and vary the voltage, but a parallel calculation, when the energy is varied and the voltage is kept fixed, results in the same characteristic resonant current variation. It is worth noting also that the resonant peaks are not as sharp as for a barrier structure.

The gain covers all three ranges as has been mentioned before. We have therefore plotted the quantum current density $\vec{j}$, visualized with arrows, for three different regions of G. In Fig. 4(a) the current is shown for $V=0.2$, where $G>1$. We clearly see here that the current circulates counter clockwise and that the current in the lower part of the structure is larger than the incoming current (i.e., compare with current i_a in Fig. 2). The fact that the current goes back is purely a quantum phenomenon. This means that an electron travels "upward" a potential hill. Classically a particle will proceed only to the output channel since the potential is lower there. This is possible because of coherence and the fact that the wave function on the right side "feels" the left side. The explanation is also analog to the case of tunneling through a barrier, something forbidden in a classical system. In Fig. 4(b) the current arrows are shown for $V=4.8$, where

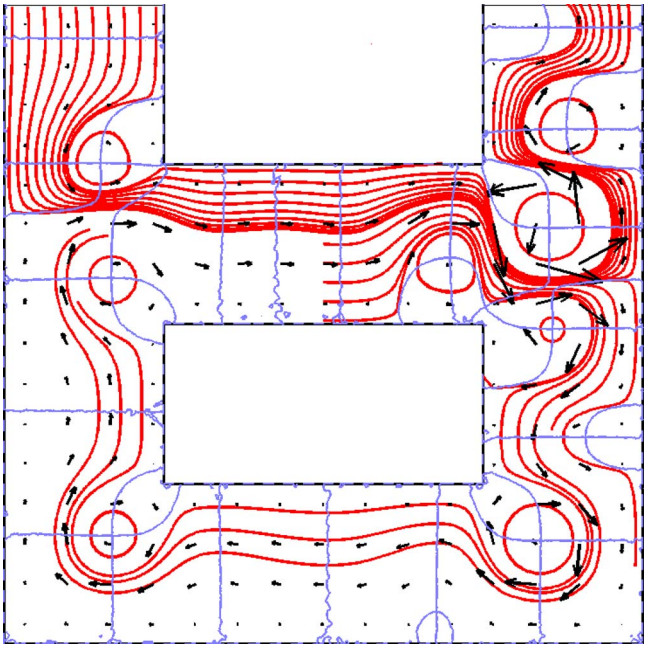

FIG. 5. (Color online) Current density (arrows) and streamlines (thick lines) obtained by the equation system $dx(t)/dt=j_x(x(t),y(t))$ and $dy(t)/dt=j_y(x(t),y(t))$. In the figure the streamlines have finite lengths (of numerical reasons); they end at different places depending on where they start. The thin lines correspond to the isolevels of $j_x=0$ and $j_y=0$. At several places we obtain so-called critical points ($j_x=j_y=0$) around where streamlines circulate. The flow goes from the input channel to the output channel via the upper branch. The lines starting from the middle of the upper branch circulate in clockwise direction.

$G=0.5$ and the current i_0 has a maximum. For this voltage, the current i_0 is divided "classically" into i_a and i_b (interpreted as probability that a billiard ball goes in one of the possible paths). Obviously, there is no effect of feedback in this case.

In Fig. 5 the current arrows and the corresponding streamlines (numerically they have finite lengths) are shown for $V=10.8$ with $G=-2$ which is very close to a current minimum (we may call this antiresonance since the current is almost equal to zero here). In this case the current is circulating clockwise. The feedback seems to be assisted by the different centers of turbulence. The thin lines in Fig. 5 shows the iso-levels of $j_x=0$ and $j_y=0$. At the points where these lines cross each other we have so-called critical points (the term critical point stems from the stability theory, established by the famed mathematician Lyapunov). Streamlines that start close to such a point will propagate in closed circular loops around this point, which can be seen in the figure, i.e., that is what we refer to as turbulence. Note also that the current density arrows near some of the critical points have a significant larger magnitude than the incoming current density arrows. In fact, one could claim that the effect of turbulence is a consequence of "local" feedback or a constructive interference of a coherent wave function.

All the discussion about feedback relies on the fact that the wave function is coherent, but in reality we know that scattering processes of various kind will destroy the coher-

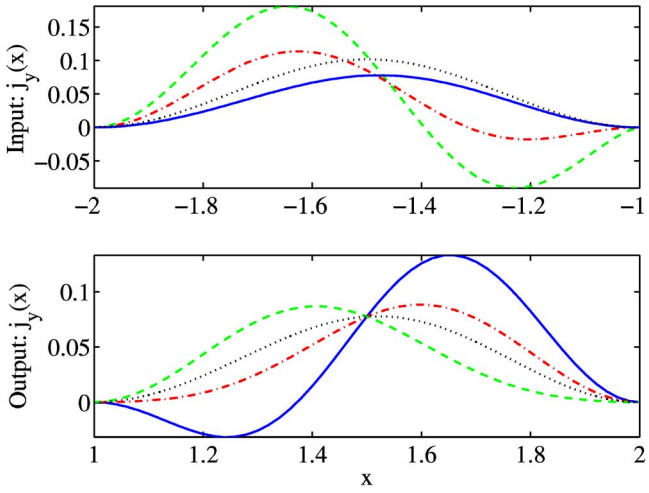

FIG. 6. (Color online) Upper figure: $j_y(x)$ shown for $y=1$ solid line, $y=0.3$ dash-dotted line, $y=0$ dashed line, and $y=2$ dotted line in the input channel (see Fig. 2 for information about coordinates). Lower figure: Current density shown for $y=1$ solid line, $y=1.2$ dash-dotted line, $y=1.6$ dashed line, and $y=2$ dotted line. $j_y(x)$ takes the ground state shape for large positive values of y (see the dotted lines in both figures). Currents above the boundaries ($y>1$) are obtained from the analytic expressions of the wave functions; meanwhile the profiles below the boundaries are interpolated form the numerical solution. It is instructive to compare $j_y(x)$ in the upper figure at $y=0$ with the current arrows and flow lines in Fig. 5 at the same position.

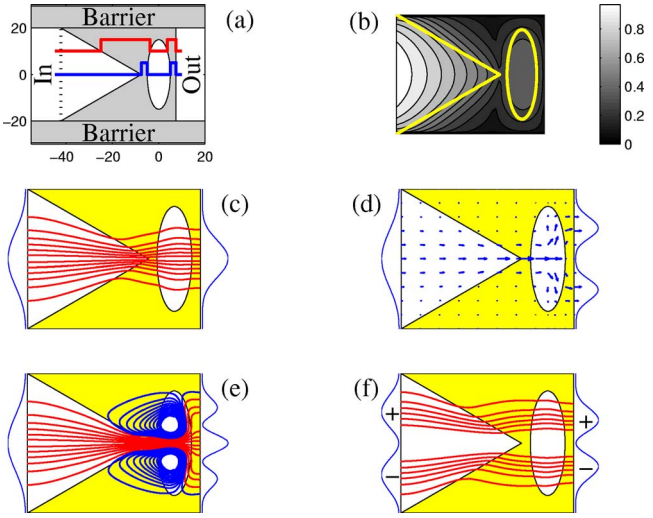

FIG. 7. (Color online) (a) The structure specifying different materials and their effective barrier potentials in the structure (barriers are gray and channels are white). The x and the y axes are oriented horizontally, respectively, vertically in the figure. The shortest distance between the tip and the ellipsoid dot is 2.5 nm. (b) Wave function $|\Psi|^{1/5}$ (grayscale), with corresponding values at the bar to the right. The potential barrier is 113 meV and the figure shows the first resonant state (see Fig. 9, $V=143.1$). (c) Streamlines for the current flow (lines) for the same case as in (b) also including current probability density $j_x(y)$ at the input and the output, boundaries (Gaussian-like functions). (d) Current density (arrows) and input and output $j_x(y)$ for $V=298.3$ between the first and the second resonant state (see Fig. 9). The flow lines are focused onto the dot via the tunnel tip, but are then divided inside the dot. (e) Laminar and turbulent (circular) current streamlines and $j_x(y)$ at the input and the output boundaries for $V=313.8$. The laminar flow lines are focused on the dot via the sharp tunnel tip but splits into three beams. The turbulent (circular) current flow is located between the tip and the right side of the dot. (f) Current streamlines and $j_x(y)$ at the antisymmetric state $2p_y$ (see Fig. 10, $V=215.8$). The current at $y=0$ is zero and due to symmetry reasons the current must go a longer distance within the barrier. A focusing effect exists in the dot.

ence. However, we believe that the destruction of coherence will be small at low temperatures. Experimentally, the existence of a magnified circular current could be detected indirectly by measuring the magnetic field close to an inner loop, for example, by using some SQUID equipment (i.e., superconductive quantum interference device, used for magnetic flux quanta detection). However, the total current is a sum of currents from many electrons with different energies and the feedback effect will, therefore, be diminished at high temperatures.

In Fig. 6, we show finally the current density $j_y(x)$ at the input and output boundaries at various positions of y, for the same situation as in Fig. 5. The total current i_0 is the line integral of $j_y(x)$ over the boundary. The upper figure shows the current density at the input boundary (at $y=1$). In the calculation we take 15 terms into account in the expression for the integro-differential boundary condition in Eq. (11), which is a very good approximation (no tracks of numerical oscillations can be seen). The output current density (lower figure) is a little bit more complicated and shows that we actually have a partial incoming current close to its left boundary. Nevertheless we see that 15 Fourier terms is fairly enough to use in the boundary condition. The use of too few terms in the Fourier sum results in an oscillation of the current density at the boundaries. The phenomenon of negative outgoing current at the output boundary could be explained by the fact that there is a turbulent center very close to it (see the critical point in Fig. 5). When we extend the output boundary outwards the channel (i.e., to $y=2$ in Fig. 2), we see that the shape of j_y is almost dominated by its boundary ground state, but this will, of course, also increase the size of the numerical grid. Actually, we can place this channel boundary at a lower position of y if we want. It is, however, easier to visualize the transport behavior by extending the channels this way.

B. Resonant dot

The investigated structure for this subsection is a thin planar structure and is shown in Fig. 7(a). The input channel extends along the horizontal axis (x axis) and has a width of 40 nm (in the vertical y direction) and it is connected to a 60° triangular tip. The triangular tip consists of the same material as the channel. The output channel has the same width as the input channel, also of the same material as the input channel. Between the tip and the output channel we have an elliptic dot with the semiradii $R_x=5$ nm and $R_y=15$ nm. The dot consists of the same material as the tip, input, and output channel. The difference in radii separates

the resonant energies between the x and the y direction. The dot is surrounded with a barrier material which is connected to the tip and the channels and we assume everywhere perfect heterojunctions. The thickness of the whole structure is taken to be 0.4 nm and it is assumed to be connected to an underlying barrier layer. Above the structure we may, for instance, assume that it is covered with an oxide cap layer (or vacuum) in which the wave function decays very quickly.

According to the one-dimensional tunneling theory, the resistance increases exponentially with the thickness of the barrier. Therefore we expect most of the current to take the shortest path through the barrier. It is also clear from the two barrier potentials, shown in Fig. 7(a) at $y=0$ and $y=10$ nm (solid lines), that the structure is a resonant tunneling structure due to the potential cavities between the two barriers.

The material for the input channel, tip, dot, and the output channel is taken to be GaAs, n-type doped with a concentration $n=2.5\times10^{16}$ cm^{-3} in the channels and no doping in the dot. This is a high concentration for this material and it is chosen to guarantee full ionization of the donors at $T=0$ (i.e., full ionization occur above the Mott-transition doping concentration, but this phenomenon refers to physics that is present in this single-particle calculation). The chosen concentration guarantees thus a metal-like characteristic at very low temperatures. For our calculation we choose $T=4.2$ K, which is a standard temperature. The concentration is also low enough for the first channel subband to play a dominating role. This means that only the ground state λ_1 (at the boundary of the input channel) gives contribution in the expression for the total current. The barrier material is taken to be $Al_{0.4}Ga_{0.6}As$ with no doping. This structure could be realized experimentally using E-beam lithography and chemical vapor deposition of Al, Ga and As to the structure. The width of the channels, the doping concentration, and the temperature are chosen this way since the calculation time is essentially reduced and also since this choice emphasizes pure quantum phenomena.

We effectively treat the problem as a two-dimensional system in the x-y plane since the thickness in the z direction is much smaller than the dimension of the structure. At low temperature and modest doping concentration of the input and output channel, the large energy separation between the ground state and the first excited state in the z direction will be so large that the ground state totally dominates, i.e., the three-dimensional wave function is taken to be $\Psi(\vec{r})=\psi(x,y)\xi_0(z)$, where $\xi_0(z)$ is the normalized ground state function in the z direction.

The used material parameters are calculated as follows. For the $Al_xGa_{1-x}As/GaAs$ interface, the band gap E_g, the conduction band offset ΔE_c, the effective mass m^*, and the dielectric constant ε are taken to be given by the empirical interpolation formulas[22]

$$E_g(x) = x3030 + (1-x)1424, \tag{35}$$

$$\Delta E_c(x) = 0.65[E_g(x) - E_g(0)], \tag{36}$$

$$\frac{1}{m^*(x)} = \frac{x}{0.15} + \frac{1-x}{0.065}, \tag{37}$$

$$\varepsilon(x) = x10.06 + (1-x)12.85, \tag{38}$$

where E_g and ΔE_c are given in meV, m^* is given in units of the electron mass and, ε is given in units of the vacuum dielectric constant (ε_0). This gives for $x=0.4$, $\Delta E_c=417.6$ meV (the barrier potential in the structure).

We use the numerical solution of the Laplace equation (the electric potential) $V(x,y)$ in the Schrödinger equation. A given voltage bias V between the input and the output channel scales the solution of the the Laplace equation. The electric field close to the tip is discontinuous and the numerical grid is therefore refined in this region (we use an adaptive solver), but the discontinuity does not affect the result since the potential is continuous. The boundary condition for the Laplace equation at the input boundary and on the tip surface is given by $V=0$, i.e., the potential in the tip is constant. The potentials at the barrier walls are taken to be of Neumann type, to mimic a realistic linear potential drop through the structure. The same argument as for the previous result section applies here also (see Sec. III A for details).

We add the barrier potential to the electrical potential, so that the effective potential used in the Schrödinger equation is given by $V(x,y)\rightarrow V(x,y)+\Delta E_c(x,y)$, where $\Delta E_c(x,y)$ is the conduction band offset.

The contour levels of the wave function $|\Psi|^{1/5}$ is shown in Fig. 7(b) for $V=143.1$ and the current streamlines are shown for the same case in Fig. 7(c). This voltage corresponds to the first resonant state as can be seen in Fig. 7(b), where $|\Psi|^{1/5}$ in the dot is relatively large and also have the 1s shape ($V=143.1$ corresponds to the first current maximum in Fig. 9). We visualize the charge density in Fig. 7(b) using the power 1/5 (of $|\Psi|$) instead of 2, since the local maximum in the dot will be visible in the grayscale contour plot (the light-gray area in the dot) for this choice of power. Current flow lines give information of the tunneling paths. The distances between the flow lines at the input boundary (in the y direction) are proportional to the current density $j_x(y)$. Both the input and the output current densities $j_x(y)$ are typically Gaussian shaped. The flow lines are focused into the dot via the sharp tunnel tip and the ellipsoid dot seems also to act as a "lens" for the incoming current; this is why the shape of the current density at the output boundary has a smaller width than the incoming distribution. If the size of the dot would have been smaller, we also expect this focus effect to become sharper, since tunneling through the dot gives "least resistance."

The input energy is low in comparison with the barrier. Therefore the wave function within the tip is a smooth function. At higher energies this changes actually and reflection at the barrier gives rise to the turbulent current in the tip region since the wavelength becomes comparable with the size of the tip.

In Fig. 7(d) the current density (arrows) is shown for voltage between the two first resonant levels. The length of the arrows are proportional to $\vec{j}(x,y)$. The current streamlines take interesting paths in this case, where the incoming beam from the tip splits into two beams. As a result, the current density at the output boundary is shaped as two separated Gaussians.

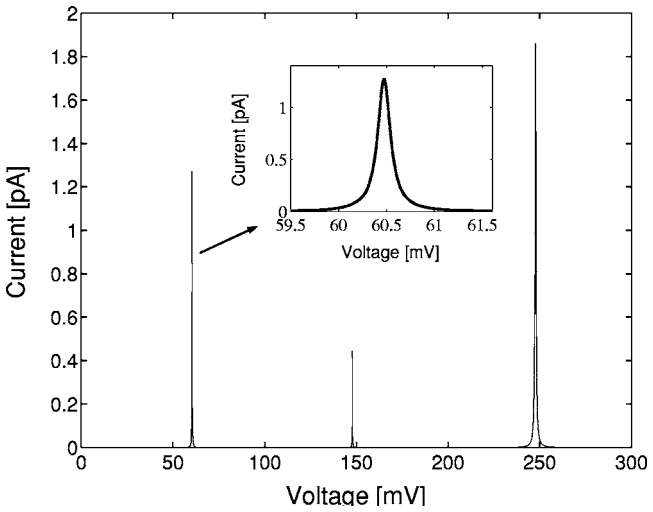

FIG. 8. I-V characteristic for tunneling through the ellipsoid dot. A zoom of the first peak shows a negative differential resistance of the order of 500 MΩ. The first state corresponds to the ground state in the ellipsoid dot. The second peak with a smaller maximum current corresponds to a symmetric eigenstate, with three $|\Psi|$ maxima along the y direction ($3p_y$). The third peak corresponds to an eigenstate with two $|\Psi|$ maxima along the x axis ($2p_x$).

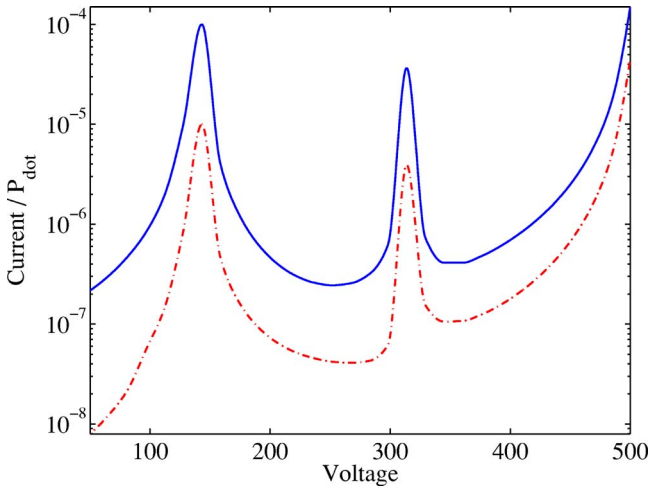

FIG. 9. (Color online) Single-electron tunnel current and relative probability to find the electron within the dot (both dimensionless) shown as a function of the voltage at a constant energy. The peaks of the resonant current and probability appear at the same kind of resonant states in the dot. The incoming wave is taken to be in the ground state of the input boundary (λ_1). The first peak corresponds to the ground state "1s" and the second peaks to the excited state $3p_y$. The resonant state $2p_x$ appears close to $V=500$.

Figure 7(e) shows the current stream for $V=313.8$ (the second peak $3p_y$ in Fig. 9). It is interesting to observe that the flow performs circular motion (i.e., turbulence) within the dot for this voltage bias. The current beam from the tip splits here into three beams, which is also indicated by the current density at the output boundary (which reminds on a diffraction pattern of light that passes through a small split).

Figures 7(b)–7(e) share in common that the wave function within the dot is symmetric. No anti symmetric state is found during the calculation. The reason for this is that the incoming wave is symmetric. The wave function in the dot cannot change phase if not the connected wave function in the tip also change phase. As a result all anti symmetric transverse resonant modes are suppressed and give no current maxima. In Fig. 7(f) we show, therefore, the current streamlines and $j_x(y)$ for the first antisymmetric channel state. The first resonant state is not the symmetric ground state for the dot, as one could have expected. Instead, the first resonant state is antisymmetric. The current density distribution at the incoming and the outgoing boundary are also reflecting this fact. The (+) and (−) in the figure indicate the phase of the wave function in respective region of the structure. We see that the current flow lines must take a much longer path through the barrier, and as a result, the current must also be much smaller than for the symmetric case (see Fig. 8 also). Note: The energy is increased for this case, to allow wavelike solutions $[\varepsilon=(\lambda_2+\lambda_3)/2]$.

The calculated I-V characteristic is shown in Fig. 8. Due to the high barrier and the low temperature the widths of the three resonant peaks are small (comparable with the thermal energy for $T=4.2$ K). A zoom of the resonant ground state peak (located at 50 mV in Fig. 8) shows that the width of the peak is about 1 meV and that the maximum current is about 1 pA. In the calculation we solve the Schrödinger equation for many wave numbers in the input channel (which thus alters the energy E), and the total current is a sum of all these values, according to the Fermi-Dirac statistics [See Eq. (34)].

The second peak in Fig. 8 corresponds to a resonant state with three $|\Psi|$ maxima, which we refer to as $3p_y$, which is symmetric with respect to the x axis. The maximum current is about 1/3 of the ground state peak. The reason for this is that only a third part of the wave function, located in the dot, is close to the tip [compared with Fig. 7(b)]. The third peak corresponds to a resonant state with two $|\Psi|$ maxima along the x axis and is referred to as $2p_x$.

Since the current is a sharp resonant function of the voltage a special procedure is used to find the maximum of the current for all values of the incoming energy, to guarantee a good precision.

In Fig. 9 we present some interesting characteristics of resonant tunneling through a barrier that is four times lower than in the previous case [the same as used in Figs. 7(b)–7(e)]. The peaks are therefore wider (than for the one obtained in Fig. 8). The solid line represents the probability P_{dot} to find the electron within the dot (in arbitrary units) and the dash-dotted line shows the single-electron current at a specific energy as a function of the bias voltage. The probability peaks correspond to resonance and it is also clear that the current maxima are strongly correlated to the probability maxima. The voltage and the current are given in scaled and dimensionless units.

In Fig. 10 the current and the probability in the dot is shown for the case when the incoming wave is in its first excited state (corresponding to the boundary eigenvalue λ_2). This eigenstate is antisymmetric with respect to the x axis. The energy is increased for this case, to allow wavelike solutions $[\varepsilon=(\lambda_2+\lambda_3)/2]$. Current and P_{dot} are calculated as a function of the voltage for a barrier $\Delta E=300$ [the same as used in Figs. 7(b)–7(f)].

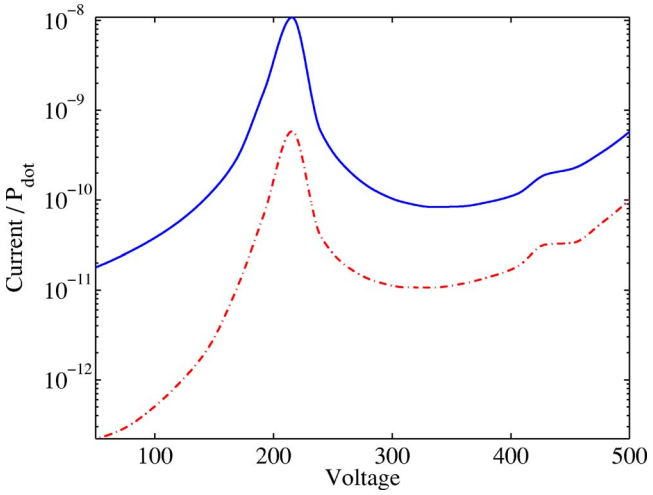

FIG. 10. (Color online) Tunnel current and relative probability to find the electron within the dot (both dimensionless) shown as a function of the voltage at a constant energy. The same calculation as in Fig. 9 but the incoming wave is taken to be in the first excited (λ_2) antisymmetric state (around the x axis) of the input boundary. The first peak corresponds to the antisymmetric state $2p_y$ (2 maxima of $|\Psi|$ in the dot) and the second little peak to the excited state $4p_y$ (4 maxima in the dot).

A comparison between Fig. 9 and Fig. 10 shows that the current for the antisymmetric case is many orders of magnitudes smaller than for the symmetric case. The reason for this is obvious when we compare Fig. 7(c)–7(f). An interesting result of this calculation is that antisymmetric resonant transverse states in the dot will contribute slightly to the I-V characteristic when the temperature becomes larger. Further on, at room temperature we expect many incoming modes to contribute with alternating symmetric and/or antisymmetric resonant current maxima in the I-V characteristic, which therefore could take a rather complex shape.

IV. CONCLUSIONS

In this paper we derive integro-differential boundary conditions for single-electron tunneling problems in complex two- and three-dimensional structures. We demonstrate the use of these conditions on two nontrivial tunneling structures. We also show how similar integro-differential boundary conditions could be obtained for plane-wave problems as well as for equations other than the Schrödinger equation (i.e., for open systems).

When we apply our boundary approach on a ringlike waveguide structure with sharp edges we show that the tunneling current is a resonant function of the applied voltage. Further on we show that this structure exhibits quantum current feedback and turbulence.

The study of a tunneling structure with a tip closely connected to an ellipsoid dot shows that the I-V characteristic is a very sharp resonant function. Current peak values, which are separated at about 100 meV, are of the order 1 pA. We explain also how resonant tunneling is obtained only for wave functions that obey certain symmetry rules. We believe that the use of our boundary approach would open new possibilities to explore rare effects within (nontrivial) electron waveguides or tunneling devices, as well as in other branches of science.

ACKNOWLEDGMENTS

The work was funded by SSF-Quantum Devices and the European SINANO project. Many thanks also to the FEMLAB support group at COMSOL, who have helped a lot in the development of the specific integro-differential boundary code.

APPENDIX: DETAILS OF BOUNDARY CONDITIONS AND NUMERICS

The numerical solution of the Helmholtz equation with the boundary conditions given in Eqs. (11) and (18) could be solved using (i) a "homemade" code for simpler geometries or (ii) finite element method softwares such as FEMLAB,[23] for instance.

Before we discuss the treatment of the boundary conditions in more detail we explain here first some basic concepts of PDE's and boundary conditions. The Helmholtz equation could be represented on the form $-\nabla\cdot(c\nabla u)+au=f$, where c, a, and f are functions of space (this is also the FEMLAB notation[23]). For the Schrödinger equation we have $c=\hbar^2/2m$, $a=V(\vec{r})-E$ (where the energy E is given), and $f=0$. The boundary conditions are usually of Dirichlet ($u=0$) or Neumann type. The Neumann boundary condition is given by $\hat{n}\cdot(c\nabla u)+qu=g$, where $\hat{n}$ is the boundary surface normal unit vector.

In Fig. 11 we illustrate how to numerically treat the integro-differential boundary condition for an output channel. For simplicity we scale our system so that $c=1$, etc. In Eq. (18) we could first put the derivative in explicit form: $\hat{n}\cdot(c\nabla u)=du/dy\approx(u_{n,1}-u_{n,2})/h$, if we use the notation $u(x_n,y_m)=u_{n,m}$. From Fig. 11 we can thus see that the numerical approximation of Eq. (18) (using only two terms in the Fourier sum) is given by

$$\frac{u_{n,1}-u_{n,2}}{h}=ih\sum_{j=1}^{7}(\kappa_1\phi_{1,n}\phi_{1,j}+\kappa_2\phi_{2,n}\phi_{2,j})u_{j,1}, \quad \text{(A1)}$$

where we approximate the integral (over x) with a Riemann sum. This equation manifests a linear relationship between different $u_{n,m}$. It differs from a normal Neumann boundary condition in the sense that a node, say $u_{3,2}$ in Fig. 11, is not only connected with $u_{3,1}$ but also to all other values of u on the boundary surface. It is interesting to note in this context that the Neumann boundary condition is a linear combination of linear operators on u. But an integral is also a linear operator on u; a more general case of a linear boundary condition could be given in the form

$$\alpha\hat{n}\cdot(c\nabla u)+\beta u+\gamma+\int_{\partial\Omega}K(\vec{r},\vec{r}')u(\vec{r}')dS'=0, \quad \text{(A2)}$$

where α,β,γ are functions of space and $\partial\Omega$ is the space of the boundary surface. The kernel $K(\vec{r},\vec{r}')$ could for Eq. (18) be identified as

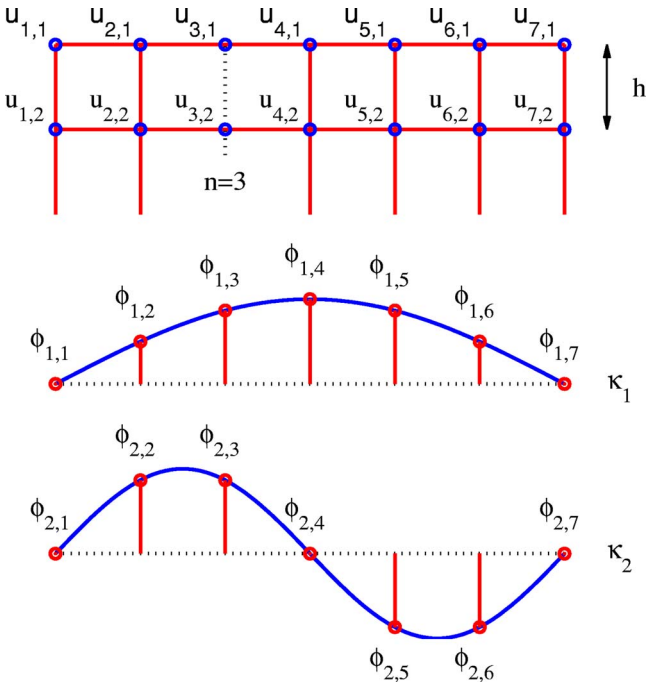

FIG. 11. (Color online) In the upper part of the figure, a numerical grid is shown close to the boundary surface for an output channel (the output channel extends above the upper line, which is the boundary surface). The variable u corresponds to the wave function in the structure (i.e., Ψ) and is on discrete form given by $u(x_n, y_m) = u_{n,m}$. The lower figures show the eigenmodes $\phi_1(x)$ and $\phi_2(x)$ with their corresponding wave numbers κ_1 and κ_2. h is the step size of the numerical grid.

$$K(\vec{r},\vec{r}') = \sum_j i\kappa_j \phi_j(\vec{r})\phi_j^*(\vec{r}'), \tag{A3}$$

if $c=1$, $\alpha = m_2/m_{\partial\Omega_2}$, and $\beta=\gamma=0$. Note that in the (hypothetical) case when $i\kappa_j=1$ we obtain the completeness relation, i.e., $K(\vec{r},\vec{r}') \to \delta(\vec{r}-\vec{r}')$. A kernel of special interest is Green's function which satisfies $(E-\hat{H})G(\vec{r},\vec{r}') = \delta(\vec{r}-\vec{r}')$, where $\hat{H}$ is the Hamilton operator. Note though that G is given in a three-dimensional space (body); meanwhile the kernel K is given in a two-dimensional system (surface). Green's functions are used extensively in the literature[7] and articles[8,9] but to the authors knowledge, they do not appear together with normal derivatives in boundary conditions such as in Eq. (A2), or explicitly as in Eq. (A1).

We describe now briefly how the boundary conditions could be treated within the finite element method based program FEMLAB. In this program it is possible to define so-called scalar integration coupling variables. Each variable is defined in the program on a specific boundary and is given a name. The output Fourier components $\hat{u}_{2j}$ are for a case similar to that shown in Fig. 11 [see also Eq. (18)] defined in the program as

$$t_j = \int \phi_j^*(x)u(x)dx, \tag{A4}$$

where we omit the complex conjugate $(*)$ in one dimension. The scalar coupling variables t_j appear then in the expression of the Neumann boundary condition as

$$\hat{n}\cdot(c\,\nabla u) + qu = i(\kappa_1\phi_1(x)t_1 + \kappa_2\phi_2(x)t_2 + \cdots), \tag{A5}$$

where $q=0$ and $c=1$ in this case. The wave numbers κ_j must be specified and also the functions ϕ_j. A similar procedure is performed for the input boundary. The geometry is drawn as in a CAD program. When the PDE coefficients, coupling variables, coefficients, and boundary conditions are specified, a grid is generated by a built in routine in FEMLAB. Finally the program is solved and the wave function and the current density will be visualized in a figure window. The solution should be specified to be given in a so-called "weak form."

To the authors knowledge, FEMLAB is the only software today that provides a direct access to the weak form of the problem, which in combination with the scalar coupling variables makes it possible to treat boundary conditions of this kind. For complex structures (i.e., nontrivial structures in two or three dimensions) with different materials regions, we believe that FEMLAB is easier to use rather than develop a specific code for it. It is more interesting to concern oneself about the physics rather than to stick into numerical problems. The mentioned FEMLAB procedure above is preferred in 2D (and 1D) and can easily be executed on a modern standard PC within seconds using a good mesh quality.

For the 3D case, this method consumes, however, a lot of computer memory (or takes too much to run), because the numerical matrix is not sparse. In this case we may use all the Fourier components as independent variables and couple them to the rest of the system. This will increase the degree of freedom of the system slightly, but the numerical matrix will be guaranteed to be sparse. Here we define pseudovariables of the Fourier components as scalar coupling variables that map the integrals on the boundaries to a point in the geometry. We have then two coupled modes, one the Helmholtz mode and one the so-called point mode (this is what is called multiphysics in FEMLAB). A set of scalar equations are specified in the point mode so that $v_{2j}-u_{2j}=0$, where v_{2j} is the independent variable, etc. Finally, we define a scalar coupling from the point back to the boundary surface, given the names $w_{2j}=v_{2j}$ where w_{2j} are used in the expression for the boundary condition (instead of t_j as in the 2D example above).

*Email address: sunkan@fy.chalmers.se

[1] R. Tsu and L. Esaki, Appl. Phys. Lett. **22**, 562 (1973).
[2] S. Luryi, Appl. Phys. Lett. **47**, 490 (1985).
[3] A. Brataas, U. Hanke, and K. A. Chao, Semicond. Sci. Technol. **12**, 825 (1997).
[4] H. Mizuta, C. Goodings, M. Wagner, and S. Ho, J. Phys.: Condens. Matter **4**, 8783 (1992).
[5] J. B. Xia and S. S. Li, Phys. Rev. B **68**, 075310 (2003).

[6] P. A. Khomyakov and G. Brocks, Phys. Rev. B **70**, 195402 (2004).
[7] S. Datta, *Electronic Transport in Mesoscopic Systems* (Cambridge University Press, Cambridge, 1995).
[8] P. Havu, V. Havu, M. J. Puska, and R. M. Nieminen, Phys. Rev. B **69**, 115325 (2004).
[9] D. Mamaluy, M. Sabathil, and P. Vogl, J. Appl. Phys. **93**, 4628 (2003).
[10] M. A. Cazalilla and J. B. Marston, Phys. Rev. Lett. **88**, 256403 (2002).
[11] J. Fransson, O. Eriksson, and I. Sandalov, Phys. Rev. B **66**, 195319 (2002).
[12] M. Mendoza and P. A. Schulz, Phys. Rev. B **68**, 205302 (2003).
[13] J. Wang and A. A. Stuchebrukhov, Int. J. Quantum Chem. **80**, 591 (2000).
[14] A. A. Starikov, I. I. Yakimenko and K-F. Berggren, Phys. Rev. B **67**, 235319 (2003).
[15] S. K. Jung, C. K. Hyon, J. H. Park, S. W. Hwang, D. Ahn, M. H. Son, B. D. Min, Y. Kim, and E. K. Kim, Appl. Phys. Lett. **75**, 1167 (1999).
[16] E. Lind, I. Pietzonka, P. Lindstrm, W. Seifert, and L.-E. Wernersson, Appl. Phys. Lett. **81**, 1905 (2002).
[17] S. Tarucha, Y. Hirayama, T. Saku, and T. Kimura, Phys. Rev. B **41**, 5459 (1990).
[18] S. Tarucha and Y. Hirayama, Phys. Rev. B **43**, 9373 (1991).
[19] M. A. Reed, J. N. Randall, R. J. Aggarwal, R. J. Matyi, T. M. Moore, and A. E. Wetsel, Phys. Rev. Lett. **60**, 535 (1988).
[20] S. Tarucha, Y. Tokura, and Y. Hirayama, Phys. Rev. B **44**, 13815 (1991).
[21] M. Tewordt, L. Martin-Moreno, V. J. Law, M. J. Kelly, R. Newbury, M. Pepper, D. A. Ritchie, J. E. F. Frost, and G. A. C. Jones, Phys. Rev. B **46**, 3948 (1992).
[22] Y. Fu and M. Willander, *Physical Models of Semiconductor Devices* (Kluwer Academic Publishers, Dordrecht, 1999).
[23] The commercial finite element method software FEMLAB is developed by the company COMSOL. Detailed information could be found on the internet address http://www.comsol.com (2005).